

Date of publication xxxx 00, 0000, date of current version xxxx 00, 0000.

Digital Object Identifier 10.1109/ACCESS.2024.0429000

# An On-body RecCoil Array Harvester System for Extended Wireless Charging of Misaligned Quadcopters

SAGAR JAIN<sup>1</sup>, (Graduate Student Member, IEEE), IGNACIO JULIO GARCIA ZUAZOLA<sup>2</sup>,(Senior Member, IEEE) and Ashwani Sharma<sup>1</sup>, (Senior Member, IEEE)

<sup>1</sup>Electrical Engineering department, Indian Institute of Technology Ropar, Punjab, India. (e-mail: sagar.20eez0013@iitrpr.ac.in, ashwani.sharma@iitrpr.ac.in)
<sup>2</sup>School of Computing and Digital Media, London Metropolitan University, N7 8DB London, U.K.(e-mail: i.garciazuazola@londonmet.ac.uk)

Corresponding author: Ignacio Julio Garcia Zuazola (e-mail: i.garciazuazola@londonmet.ac.uk).

This work was supported in part by NMICPS TIHAN Foundation IIT Hyderabad.

ABSTRACT In conventional unmanned aerial vehicle (UAV) wireless charging systems, the quadcopter must be perfectly aligned with the charging pad to ensure effective magnetic coupling for charging. To enhance quadcopter landing flexibility, the authors propose an innovative on-body RecCoil array harvester with a central receiver (Rx) coil to capture longitudinal field components and four auxiliary side Rx coils to encapsulate lateral field components, each formed by two oppositely wound circular coils and integrated with full-bridge rectifiers. The rectified outputs are combined using a DC technique. The Rx coil is EMoptimized to harness three orthogonal H-field components from the Tx coil, ensuring uniform voltage and Power Transfer Efficiency (PTE) across the Rx plane at a 50 mm altitude. Simulation results indicate that the lateral misalignment tolerance of the proposed structure decreases with increasing altitude beyond 50 mm. The design improves measured PTE to 72.22% (aligned) and 70.91% (misaligned), outperforming the conventional Rx coil's PTE of 50.13% and 17.01%, respectively. Furthermore, it is seamlessly integrated with the PCB-based charging circuitry to validate and demonstrate the battery charging process effectively. Because it weighs 20 g lower than its competitors, its flying efficiency won't be compromised, thereby providing a superb misalignment charging (offset between the Tx and Rx) of 100% at 50 mm for the quadcopter with good PTE, given the well-organized and optimized RecCoils to well-matched full AC-DC rectification. The dynamic tests for drone charging will be considered as a part of future works.

**INDEX TERMS** Coil antenna, lateral misalignment, magnetic resonant coupling, misalignment tolerance, rectifier, wireless power transfer, battery charging.

### I. INTRODUCTION

N the current era, quadcopters are becoming increasingly popular due to their deployment in various fields such as package delivery [1], agricultural monitoring [2], medical emergencies [3], and defense surveillance [4]. However, the utility of quadcopters in these applications is limited by their restricted flying time, primarily due to the use of conventional batteries that require frequent human intervention for replacement. This traditional battery replacement is not feasible in remote areas. One solution to enhance quadcopter autonomy is the installation of solar panels on the quadcopter wings to charge the batteries, but this approach is impractical in cloudy conditions. Further, this method causes instability and increased drag during the quadcopter flight [5]. Another method

involves charging the quadcopter via metal contacts, which requires perfect alignment for efficient charging and also possesses safety risks such as short circuit and overheating. An alternative and more effective solution is to wirelessly charge quadcopters using wireless power transfer (WPT) through Magnetic Resonance Coupling (MRC) [6]–[8].

In MRC, power is wirelessly transferred from a transmitter (Tx) coil to a receiver (Rx) coil, with capacitors inserted in both coils to achieve resonance and maximize power transfer efficiency (PTE). However, coaxial misalignment of the Rx coil with the Tx coil, known as lateral misalignment, significantly reduces PTE due to decreased flux linkage with the Rx coil [9]. A conventional approach to address this issue involves using an automated robotic system to align the Rx



coil coaxially with the Tx coil [10]. Nevertheless, this method suffers from wear and tear, increased maintenance, and high system costs. Another solution is to incorporate complex hybrid compensation networks to stabilize the current in the Tx coil despite varying load conditions [11]-[13]. Still, this approach increases complexity and net effective resistance. Additionally, it does not ensure uniform induced voltage across the Rx plane. An alternative involves deploying a ferrite core in the Tx coil to enhance magnetic flux linkage with the Rx coil [14], [15]. However, this increases system costs and introduces eddy current and hysteresis losses. Various authors have proposed a more practical solution using fieldforming techniques to mitigate lateral misalignment. One method optimizes Tx coil parameters to achieve a uniform magnetic field [16]. Similarly, a quasi-elliptic Tx coil was developed in [17] to achieve stronger coupling over a larger area in the Rx plane. However, these methods suffer from significant magnetic flux leakage. Another attempt to achieve a uniform H-field is described in [18], where a 3-D Tx coil design consists of two orthogonal coil structures. This method increases the net resistance in the Tx coil and causes high flux leakage for a small Rx coil on the quadcopter body, increasing eddy current losses. All the afore-mentioned techniques suffer from degraded PTE. Therefore, switchable Tx coils were deployed in [19], [20], where sensors detect the misaligned Rx coil and actuate an appropriate set of Tx coils. Although this arrangement mitigates flux leakage, it suffers from increased system complexity, cost, and a high failure rate due to the use of switches and sensors. Despite efforts to sophisticate Tx coils, the planar Rx coil can only harness the longitudinal field component, leading to ineffective H-field encapsulation. Consequently, Rx coil structures have been modified to address this issue.

An origami-based Rx coil was designed in [21], where copper tapes were adhered to paper to create both the Tx and Rx coils. Although this design is lightweight and minimally impacts the quadcopter's payload capacity, it offers limited mitigation for lateral misalignment. In [22], [23], a 3-D Rx coil was geometrically optimized to improve the error tolerance for quadcopter misalignment. Additionally, a Rx coil made from aluminum foil was designed in [24] to reduce its impact on the quadcopter's payload capacity and air drag. However, the Rx coils in these studies can only capture the longitudinal  $(H_z)$  field component. To overcome the limitations posed by traditional receiver (Rx) coil configurations in wireless quadcopter charging, a 3-D squirrel cage structure was proposed in [25] to harness both the longitudinal and one lateral H-field component  $(H_x \text{ or } H_y)$ . While this marked an advancement, the induced voltage in this structure varies significantly with lateral misalignment, leading to unstable charging and reduced battery lifespan. Building on this, a hollow aluminum tube-based 3-D Rx coil was introduced in [26] to capture all three orthogonal H-field components. Although it also served as a mechanical support for quadcopter landing, the design incurred considerable eddy current losses due to the large metallic surface area, causing heat dissipation and degradation in power transfer efficiency (PTE). Moreover, its optimization was limited to the aligned configuration and did not address misalignment scenarios. A mortarboard-shaped 3-D Rx coil presented in [27] offered further improvements in capturing the complete H-field, yet its bulky structure is incompatible with the limited clearance under most quadcopters, underscoring the need for planar, low-profile 2-D Rx coil architectures. Among planar solutions, very few studies, such as [23], attempt to mitigate the impact of lateral misalignment through voltage combining techniques. However, the misalignment tolerance achieved remains modest. Early explorations using anti-parallel coil configurations—where two coils are wound in opposite orientations—were reported in [28], mainly in the context of transmitter (Tx) coils [29], [30] to stabilize mutual inductance and operating frequency. The use of such a configuration at the Rx side to capture lateral fields was investigated in [28], [31], supported by the reciprocity theorem of antennas [32]. Nonetheless, these designs were optimized only for the aligned case, exhibited sensitivity to misalignment, and lacked rectification or integration with charging circuits. To overcome these gaps, the authors propose a novel, fully integrated RecCoil array system— an optimized 2-D Rx architecture composed of a central Rx coil for longitudinal field capture and four auxiliary anti-parallel side coils for lateral field harvesting. Each coil is independently tuned and rectified, and the rectified outputs are combined at the DC level to ensure constructive voltage addition regardless of misalignment. Unlike previous 2-D designs, the proposed system is optimized using electromagnetic simulation to achieve 100% misalignment tolerance along the axis (MTA) in both X and Y directions at a fixed altitude of 50 mm, while maintaining a stable and high-efficiency DC output. Fabricated using lightweight Litz wire, the RecCoil array is cost-effective, mechanically compatible with quadcopter landing gear, and minimally affects payload capacity—advantages unattainable by prior 3-D Rx coil systems. Finally, the design is validated through successful experimental integration with a PCB-based battery charging circuit, confirming its effectiveness for real-world drone charging applications.

This manuscript consists of five sections. Section II describes the structural layout and circuit representations of the RecCoil array harvester structure. Whereas, Section III describes in detail the optimization procedure and outlines the final layout for the Tx and RecCoil array harvester structure. Section IV describes the experimental setup and discussion on load voltage, PTE uniformity and battery charging. The paper is finally concluded in Section V.

## II. STRUCTURAL LAYOUT OF THE PROPOSED RECCOIL ARRAY HARVESTER

The WPT system, consisting of a conventional Tx and the proposed RecCoil array harvester system for quadcopter charging, is depicted in Fig. 1. The square Tx coil is characterized by a side length  $S_{Tx}$ , number of turns  $N_{Tx}$ , and is excited with current  $I_{Tx}$ . This setup emits  $H_x$ ,  $H_y$  and  $H_z$  field components.

The former is captured by the conventional central Rx coil, with radius  $R_C$ , located beneath the quadcopter main frame at an altitude  $h_C$ . In contrast, latter is harvested by auxiliary side Rx coils-i, which consist of two circular coils of radius  $R_{SRi}$ , connected with opposite windings, where  $i \in [1,4]$ . They are attached to quadcopter landing gear at height  $h_{SRi}$  with their common junction at  $S_H$  distance away horizontally from the centre of the conventional Rx coil. Each Rx coil is equipped with a resonating capacitor and integrated with a bridge rectifier, filter capacitor and by-pass diode to convert the induced AC voltage into DC voltage, which is then constructively combined in series to provide the final output voltage across the battery charging circuitry, which is used for powering the quadcopter's battery. The Tx and Rx coils have a homogeneous trace width of w.

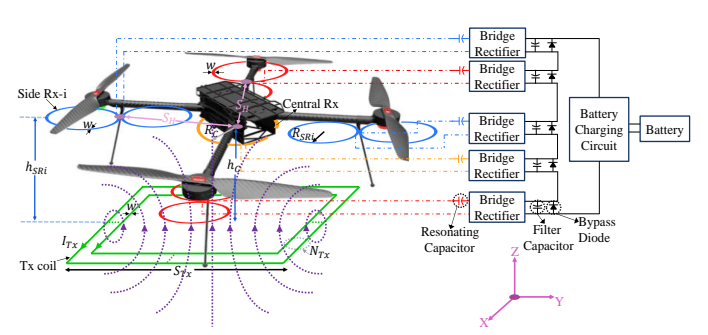


FIGURE 1. Scenario of the RecCoil array harvester for quadcopter charging.

The motivation for employing anti-parallel coils as side Rx coils to achieve a uniform load voltage in the proposed RecCoil array harvester system is illustrated in Fig. 2. The anti-parallel coils are wounded with concentrated turns to ensure efficient lateral H-field harnessing. When the RecCoil system is perfectly aligned with the Tx coil, as shown in Fig. 2(a), the central Rx coil harnesses the  $H_z$  field lines, which are parallel to its area vector and dominant at the center, thereby generating a larger induced voltage than that by side Rx coils by virtue of Faraday's law of electromagnetic induction [33]. However, when the array harvester system is laterally misaligned from the Tx coil center by  $\Delta y_r$  along the positive Y-axis, depicted in Fig. 2(b),  $H_z$  field diminishes, leading to a significant reduction in its induced voltage and a degraded PTE. Conversely, the side Rx coil-3 closely aligns with the Tx coil edges, where the  $H_v$  field is at its peak, thus harnessing it and attaining its increased induced voltage to compensate for the decrement in induced voltage from the central Rx coil. Similarly, when the RecCoil system is laterally misaligned along -Y axis or  $\pm X$ -axis, side Rx coil-1 and 2/4 compensates for the reduction in the net induced voltage, respectively.

The circuit diagram of the proposed WPT system, including the Tx coil and RecCoil array harvester, is shown in Fig. 3. The Tx coil is driven by a sinusoidal voltage source with amplitude  $V_S$  and source resistance  $R_S$ , resulting in a current  $I_{Tx}$ . It is characterized by resistance  $R_{Tx}$  and induc-

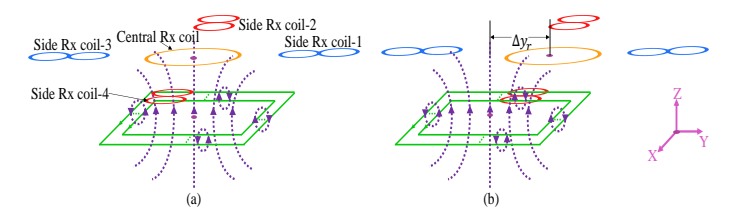


FIGURE 2. Proposed WPT structure with RecCoil harvester under (a) perfect alignment (b) misaligned condition along Y-axis.

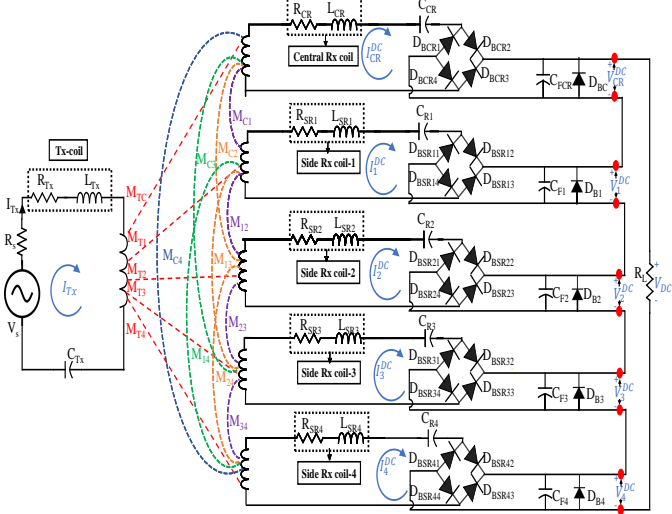


FIGURE 3. Circuit representation of the proposed WPT system containing Tx and the RecCoil array harvester.

tance  $L_{Tx}$ . To achieve resonance at the operating frequency  $f_o$ , a compensation capacitor  $C_{Tx}$  is employed in series with the Tx coil. Similarly, the RecCoil array harvester system comprises the central Rx coil and side Rx coils, each with resistances  $R_{CR}$  and  $R_{SRi}$  and inductances  $L_{CR}$  and  $L_{SRi}$ . The coils are tuned with compensation capacitors  $C_{CR}$  and  $C_{Ri}$ . Mutual inductances between different coils are manifested as  $M_{jk}$ , where j, k = C, 1, 2, 3, 4 and  $j \neq k$ . Diodes  $DBCR_j$  and DBSRii are arranged in bridge form to convert the induced AC voltage in each Rx coil to pulsating DC voltage, where  $j \in [1, 4]$ . To filter out voltage ripples from the output of each Rx coil, filtering capacitors  $C_{FCR}$  and  $C_{Fi}$  are connected in shunt. Additionally, bypass diodes  $D_{BC}$  and  $D_{Bi}$  are included to prevent any under-harvesting Rx coil from behaving as a load. The individual DC voltages generated by each RecCoil are then constructively combined in series to produce the overall DC voltage across  $R_L$ . It is crucial to note that the coils are not connected in series and then rectified, as this would result in the destructive addition of individual coil voltages, thereby diminishing the overall load voltage. Mathematically, the net voltage across  $R_L$  can be expressed as

$$V_{DC}(\Delta x_r, \Delta y_r) = (|V_{CR}^{DC}(\Delta x_r, \Delta y_r)| + |V_1^{DC}(\Delta x_r, \Delta y_r)| + |V_2^{DC}(\Delta x_r, \Delta y_r)| + |V_3^{DC}(\Delta x_r, \Delta y_r)| + |V_4^{DC}(\Delta x_r, \Delta y_r)|.$$
(1)

To achieve uniform induced voltage along both X and Y dimensions of the Rx plane at an altitude of 50 mm, various



geometrical parameters of the Rx coil are adjusted. The procedure for optimizing the Tx and Rx coil structures is detailed in the section III.

## III. OPTIMIZATION PROCEDURE OF COILS AND THE PROPOSED COIL LAYOUT

The design was simulated using an EM simulator to manually optimize the Tx and Rx coil geometry to achieve full misalignment oblivion along the X and Y axis at the operating frequency of 100 kHz. The justification for the choice of 100 kHz frequency is explained as follows. Operating at substantially low frequency for the near-field WPT system requires large-sized Tx and Rx coils to maintain the same mutual inductance; therefore, it will increase system weight, reducing the drone's payload capacity. On the contrary, higher frequencies in the order of MHz will entail substantial switching losses, thereby requiring the deployment of the expensive GaN-based inverter to maintain efficiency [34]. Further, the coils may become electrically large at higher frequencies and do not constructively support the induction mechanism. Moreover, the 85-300 kHz frequency band is also a chosen frequency standard for drone charging near-field WPT [5].  $S_{Tx}$  of the square Tx coil is fixed to 127.2 mm, with  $w_T =$ 1.2 mm to achieve maximum H-field at the Rx plane at an altitude of 50 mm [35]. To ensure the  $H_z$  field magnitude remains within the 21 A/m limit according to ICNIRP guidelines [5], [36], a parametric sweep on  $N_{Tx}$  is first performed, as illustrated in Fig. 4. Therefore,  $N_{Tx}$  is determined to be 6. The 3-D  $H_z$ -field profile generated by the optimized Tx coil is illustrated in Fig. 5(a). It is observed that  $H_z$  field diminishes with increase in distance from the point  $(x_r, y_r) = (0, 0) mm$ . Consequently, any misalignment of the quadcopter from the Tx coil center significantly reduces the induced voltage in the central Rx coil, impairing wireless quadcopter charging efficiency.

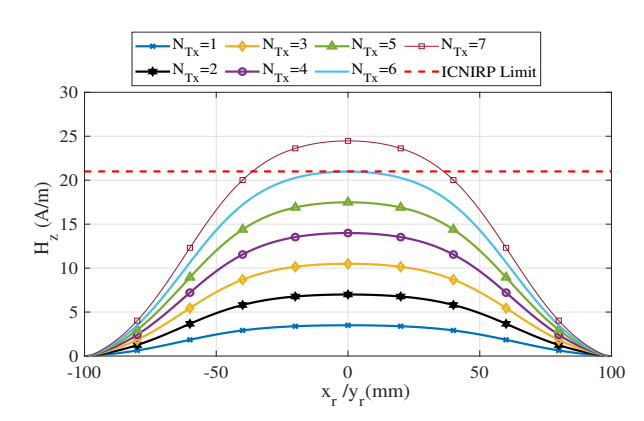


**FIGURE 4.** The  $H_z$  field distribution in the Rx plane at 50 mm altitude with varying Tx coil turns  $N_{Tx}$ .

In contrast, the  $H_x$  and  $H_y$  fields peak at  $(\pm 63.6, 0)$  mm and  $(0, \pm 63.6)$  mm with a magnitude of 12.55 A/m, as observed in Fig. 5(b) and (c), respectively. Therefore, additional side-Rx coils are needed to capture them, ensuring that the total voltage of the overall Rx coil structure does not deterio-

rate with lateral misalignment. Since the maximum  $H_x/H_y$  magnitude is significantly less than the maximum amplitude of  $H_z$ , intuitively a large size for the side antiparallel coil is required to generate comparable induced voltage when the coils are laterally displaced along  $x_r/y_r$ -axis [27]. This approach ensures optimal energy harvesting for quadcopter charging despite potential offset of the quadcopter relative to the Tx coil. It is important to note that the side Rx coils must be positioned symmetrically with respect to the quadcopter frame, which has less effect on the quadcopter stability due to the placement of coils in the frame and drone legs.

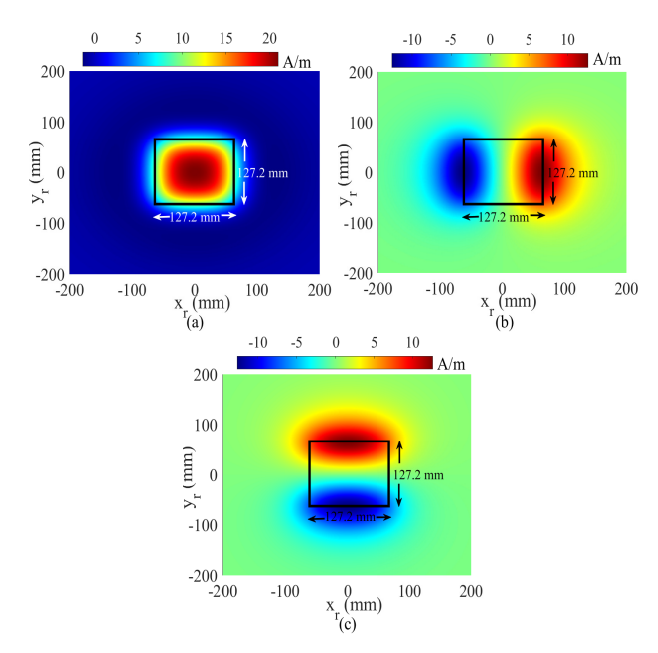


FIGURE 5. The (a)  $H_z$  (b)  $H_x$  (c)  $H_y$ -field distribution in the Rx plane at 50 mm altitude due to the Tx coil of  $S_{7x}=127.2$  mm.

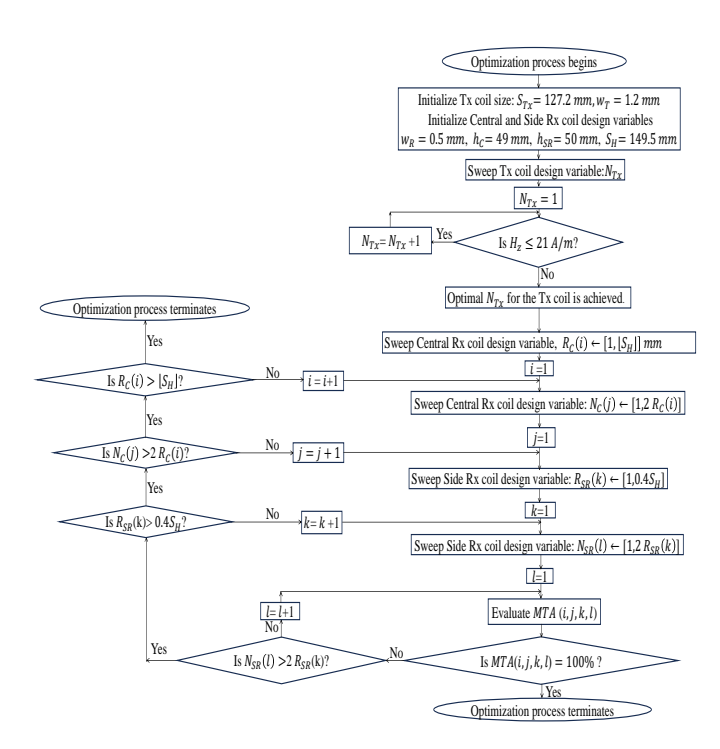
The geometry of the Rx coils is optimized using an EM simulator to maximize voltage uniformity along  $x_r$  and  $y_r$  dimensions. To evaluate the performance of the Rx coil structure, a metric called Misalignment Tolerance along the axis (MTA) is used. MTA is defined as the ratio of the extent of the misalignment tolerance along the  $x_r/y_r$  axis (where  $V_{DC}(\Delta x_r, \Delta y_r)$  lies within  $\pm 5\%$  of  $V_{DC}(0,0)$ ) to  $S_{Tx}$ .

To simplify the optimization process and reduce the simulation time, the geometrical parameters  $R_{SRi}$  and  $h_{SRi}$  are taken as  $R_{SR}$  and  $h_{SR}$ , correspondingly. In order to optimize the entire Rx coil structure, design variables  $R_C$ ,  $N_C$ ,  $R_{SR}$  and  $N_{SR}$  are parametrically swept sequentially to achieve a MTA of 100%. The detailed optimization procedure is provided below and is also depicted in the form of a flowchart in Fig. 6.

The detailed steps to obtain the optimized geometry for the Tx and Rx coils are mentioned below:

**Step 1**: Initialize Tx and Rx coil design parameters  $S_{Tx} = 127.2 \text{ mm}$ ,  $w_T = 1.2 \text{ mm}$ ,  $w_R = 0.5 \text{ mm}$ ,  $h_C = 49 \text{ mm}$ ,  $h_{SR} = 50 \text{ mm}$ ,  $S_H = 149.5 \text{ mm}$ . Distinct values of  $h_C$  and  $h_{SR}$  are chosen to prevent the possible overlap of central and side Rx coils. The value of  $S_H$  is determined by the typical





 $\begin{tabular}{ll} \textbf{FIGURE 6.} & \textbf{Flow} chart for obtaining the optimized Tx and Rx coil geometries. \end{tabular}$ 

distance from the commercial quadcopter landing gear to its center.

- **Step 2**: Sweep the Tx coil design variable  $N_{Tx}$ .
- **Step 3**: Verify the condition on  $H_z$  to ensure  $H_z < 21 A/m$ . Repeat step-2 and 3 until the condition fails.
- **Step 4**: The range of  $[1,\lfloor S_H\rfloor)$ ] is swept for central Rx coil design variable  $R_C$ . It is stored in the vector  $R_C(i)$  as  $R_C(i) \Leftarrow [1,\lfloor S_H\rfloor]$ . Here,  $\lfloor S_H\rfloor$  represents the greatest integer less than or equal to  $S_H$ . The upper limit of  $\lfloor S_H\rfloor$ ) is restricted to prevent the overlap of the central Rx coil with the landing gear of the quadcopter.
  - **Step 5**: Initialize i = 1 to call individual  $R_C$  values.
- **Step 6**: For each fixed  $R_C$ , vary the turns  $N_C$  in the range of  $[1,2R_C(i)]$  and fetch in vector as  $N_C(j) \Leftarrow [1,2R_C(i)]$ . The upper range of  $N_C$  is capped to prevent the overlap of the coil turns.
  - **Step 7**: Initialize j = 1 to summon individual  $N_C$  values.
- **Step 8**: Perform the parametric sweep for the side Rx coil dimensions  $R_{SR}$  from 1 to 0.4  $S_H$  and fetch in vector  $R_{SR}(k)$ . Its upper range is limited to prevent overlapping of side relay coils.
  - **Step 10**: Initialize k = 1 to call  $R_{SR}$  values.
- **Step 11**: Parameterize  $N_{SR}$  within the range of  $[1,2R_{SR}]$  and accumulate them in vector  $N_{SR}(l)$ .
  - **Step 12**: Initiate l = 1 to sweep  $N_{SR}$  values.
- **Step 13**: Evaluate *MTA*. Examine if 100 % *MTA* is achieved. If not, then proceed to the next step. Otherwise, the optimized geometrical parameters for the central and side Rx coils are obtained and the optimization process terminates here.

- **Step 14**: Scrutinize the condition on  $N_{SR} > 2R_{SR}$ . If the condition fails, increment the index l by 1 and rerun Step 11-14. Otherwise, proceed to the next step.
- **Step 15**: Check if  $R_{SR} > 0.4S_H$ . If the condition is not satisfied, increase the index k by 1 and reperform Step 8-15. Otherwise, go to next step.
- **Step 16**: Examine the condition on  $N_C > 2R_C$ . When the condition fails, increase index j by 1 and redo Steps 6-16. Otherwise, go to next step.
- **Step 17**: Inspect whether  $R_C > \lfloor S_H \rfloor$ . When the condition fails, increase the index by 1 and re-execute steps 4-17. Else, go to next step.
- **Step 18**: If  $MTA\ 100\%$ , then the optimized side Rx coil parameters are obtained. The optimization process terminates here. In other words, the convergence of the results are verified by the following equation

$$|MTA(i, j, k, l) - 100| = 0$$
 (2)

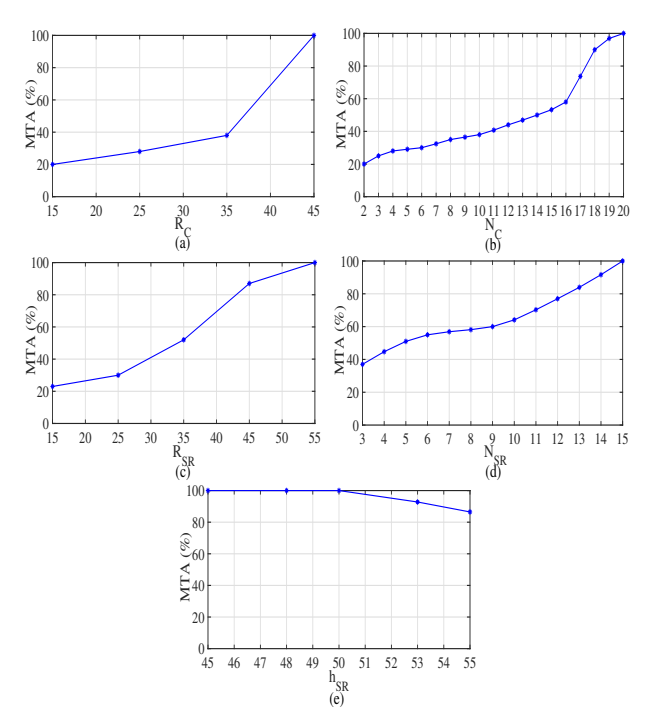


**FIGURE 7.** Plot of *MTA* versus (a)  $R_C$  with fixed  $N_C = 20$ ,  $R_{SR} = 54$  mm,  $N_{SR} = 15$ , (b)  $N_C$  with fixed  $R_C = 45$  mm,  $R_{SR} = 54$  mm,  $N_{SR} = 15$ , (c)  $R_{SR}$  with fixed  $R_C = 45$  mm,  $N_C = 20$ ,  $N_{SR} = 15$ , (d)  $N_{SR}$  with fixed  $N_C = 20$ ,  $R_{SR} = 54$  mm,  $N_{SR} = 15$ . (e) Height with optimized geometrical parameters.

The parametric variation results for the (MTA) with respect to  $R_C$ ,  $N_C$ ,  $R_{SR}$ , and  $N_{SR}$  are presented in Fig. 7(a)–(d). Although a comprehensive evaluation was conducted to examine the MTA across a broad range of coil dimensions, the results presented here focus on individual parametric sweeps, where one parameter is varied at a time while the others are held constant at their optimized values. In Fig. 7(a), the variation of MTA with central coil radius  $R_C$  is shown for  $N_C = 20$ ,  $R_{SR} = 54$  mm, and  $N_{SR} = 15$ . The MTA increases approximately linearly as  $R_C$  increases from 15 mm



TABLE 1. Geometrical Parameters of Tx and various Rx coils

Tx and Rx coil dimensions					
$S_{Tx}/R_C/R_{SR}$ (mm)	127.2/45/54				
$N_{Tx}/N_C/N_{SR}$	6/20/15				
$w_T/w_R (mm)$	1.2/0.5				
Height and Positioning of Rx coils (mm)					
$h_C$	49				
$h_{SR}$	50				
$S_H$	149.5				

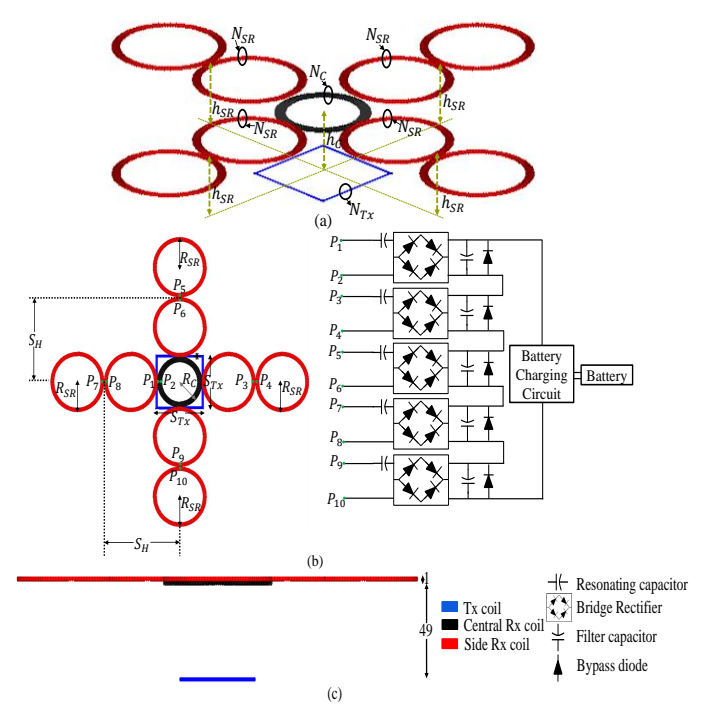


FIGURE 8. (a) 3-D view (b) Top view with DC combining technique at the right side (c) Side view of the proposed RecCoil array harvester System.

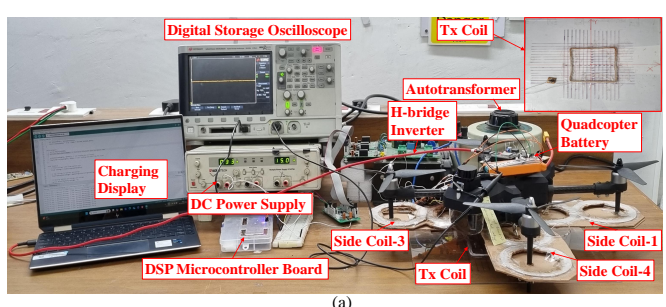
to 35 mm, with a more pronounced rise observed beyond this range. Fig. 7(b) illustrates the dependence of MTA on the number of turns in the central coil  $N_C$ . A linear increase is observed up to  $N_C = 16$ , after which a sharp rise in MTA is noted. Fig. 7(c) presents the variation of MTA with the side-coil radius  $R_{SR}$ , keeping  $R_C = 45 \text{ mm}, N_C = 20$ , and  $N_{SR} = 15$  constant. A steady increase in MTA is observed across the considered range, as the increased size in side Rx coils contribute to greater induced voltage. This increase effectively compensates for the reduction in induced voltage from the central Rx coil caused by lateral misalignment. Similarly, Fig. 7(d) shows the effect of varying  $N_{SR}$ , with fixed values of  $R_C = 45$  mm,  $N_C = 20$ , and  $R_{SR} = 54$  mm. The MTA exhibits a consistent increase with rising  $N_{SR}$ . Fig. 7 (e) illustrates the variation of the MTA with the height  $h_{SR}$  for the proposed structure with optimized parameters, specifically  $R_C = 45 \text{ mm}, N_C = 20, R_{SR} = 54 \text{ mm} \text{ and } N_{SR} = 15. \text{ It}$ is observed that the MTA remains at 100% with  $h_{SR}$  up to 50 mm; however, it begins to decline almost linearly at a constant rate of approximately -2.71 as  $h_{SR}$  increases. The design

TABLE 2. Simulated Mutual inductance between Tx, Central and Side Rx coils (in  $\mu H$ )

$M_{TC}$	5.52	$M_{T1}$	0.97	$M_{T2}$	0.96
$M_{T3}$	0.95	$M_{T4}$	0.97	$M_{C1}$	0.74
$M_{C2}$	0.75	$M_{C3}$	0.75	$M_{C4}$	0.73
$M_{12}$	0.39	$M_{13}$	0.50	$M_{14}$	0.42
$M_{23}$	0.74	$M_{24}$	0.31	$M_{34}$	0.46

parameters of Tx, central and auxiliary Rx coils, obtained through the optimization process, are summarized in Table 1. The resulting optimized layout of the proposed RecCoil array structure represented in 3-D view is depicted in Fig. 8(a). Fig. 8(b) illustrates its top view. Here, each  $P_{2m-1} - P_{2m}$  coil terminal is connected to compensation capacitor followed by a bridge rectifier, filter capacitors and bypass diodes to obtain individual DC voltage where  $m \in [1,5]$ . These are then combined constructively to yield net voltage across the load consisting of battery charging circuit to charge the battery. The side view of the proposed layout is shown in Fig. 8(c). The simulated values of the mutual inductance between various coils is provided in Table 2. The realization of this prototype along with simulated and experimental results are discussed in section IV.

#### IV. EXPERIMENTAL RESULTS AND VALIDATION



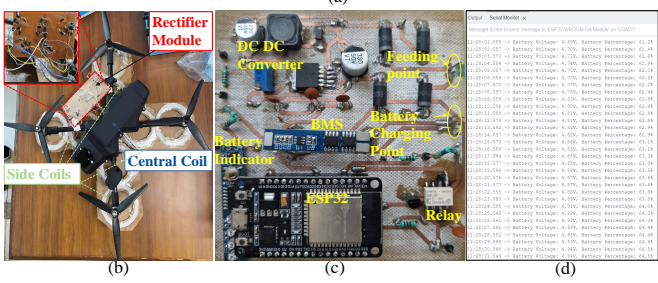


FIGURE 9. (a) Experimental setup for the proposed WPT system. (b) Top View of the RecCoil array harvester setup on the quadcopter. (c) Battery charging circuitry realized on PCB. (d) Battery voltage readings displayed in Serial Monitor indicating charging status.

The Tx, central, and side anti-parallel Rx coils are wound using Litz wires of SWG 37 and 40, respectively, each comprising 25 strands. These Litz wires consist of enameled copper conductors with a base coating of polyurethane or polyesterimide and a top coating of aromatic polyamide. They are specifically engineered to mitigate skin and proximity effects up to 1 *MHz* frequency and are thermally rated to



TABLE 3. Measured Impedance (Z), Inductance (L) for Tx, Central and Side Rx Coils

Coil Name	$R(\Omega)$	$L(\mu H)$
Tx Coil	1.41	15.72
Central Rx Coil	1.12	42.62
Side Rx Coil-1	1.09	93.65
Side Rx Coil-2	1.21	91.26
Side Rx Coil-3	1.02	94.69
Side Rx Coil-4	1.10	94.9

TABLE 4. Measured Mutual inductance between Tx, Central and Side Rx coils (in  $\mu$ H)

$M_{TC}$	6.57	$M_{T1}$	1.33	$M_{T2}$	1.29
$M_{T3}$	1.21	$M_{T4}$	1.23	$M_{C1}$	0.50
$M_{C2}$	0.46	$M_{C3}$	0.45	$M_{C4}$	0.42
$M_{12}$	0.39	$M_{13}$	0.50	$M_{14}$	0.42
$M_{23}$	0.45	$M_{24}$	0.49	$M_{34}$	0.46

withstand temperatures ranging from 155 °C to 240°C and offers enhanced immunity against moisture [37]. The Tx coil is enclosed in a non-conductive transparent plastic housing for the actual prototype, with no metallic parts that could influence the magnetic field distribution. The experimental setup, depicted in Fig. 9(a), consists of an auto-transformer to regulate the AC power supply, which is subsequently rectified to produce a DC signal. This DC signal is fed into a single-phase H-bridge inverter (model VP000218) with  $R_S = 0.013 \Omega$ . Additionally, a DC power supply powers the DSP microcontroller board (TMS320F28379D), enabling it to generate control signals for the H-bridge inverter. The inverter generates a 100 kHz AC square wave signal that is fed to the Tx coil. According to Faraday's law of electromagnetic induction, an AC voltage is induced in each Rx coil, which is subsequently rectified using a full-bridge rectifier comprising four 1N5821 diodes, a 480 µF filter capacitor and bypass diode (1N5821). This configuration exemplifies a primary-side power control scheme commonly used in WPT systems [38]. The impedances and inductances of the Tx and Rx coils are measured at the operating frequency  $(f_a)$  using an Aplab LCR Meter, with the values detailed in Table 3. A surface-mount device (SMD) capacitor with a value of 19.21 nF is used as the compensation capacitor for the Tx coil. In contrast, capacitors of 59.78 nF and 26 nF are employed for the central and side Rx coils, respectively. The weight of the Tx and Rx coils was measured using a precision weighing balance. The Tx coil weighed 22 g, the central Rx coil weighed 38 g, and each of the four side Rx coils weighed approximately 58 g, as they are geometrically identical. These weight measurements are essential for evaluating the structural loading of the Rx coils when integrated beneath the drone chassis, where the central Rx coil is mounted below the drone frame and side Rx coils are mounted symmetrically along the drone legs.

The top view of the RecCoil array harvester coils integrated with the quadcopter landing gears, with the central Rx coil positioned beneath the main frame of the quad-

copter, is shown in Fig. 9(b). The rectified output is then passed to the feeding point of the battery charging circuit realized on printed circuit board, which includes DC-DC (Buck) converter and an embedded ESP32 microcontroller for monitoring the quadcopter's battery status and facilitating the charging process. This prototype is depicted in Fig. 9(c). Initially, the microcontroller isolates the charging circuit from the rest of the Rx circuitry using a relay (OMRON 19YOYH G6K-2F), allowing it to monitor the battery's current status. The status is displayed on the Serial Monitor of the Arduino IDE, as illustrated in Fig. 9(d). If the battery voltage drops below the minimum threshold of 3.5 V, a charging request is triggered, and the relay connects the drone battery to the RecCoil array harvester output voltage, initiating the charging process. The Battery Management System (BMS) is embedded to prevent the quadcopter battery from short circuit protection, over-discharge protection, and over-current protection [39].

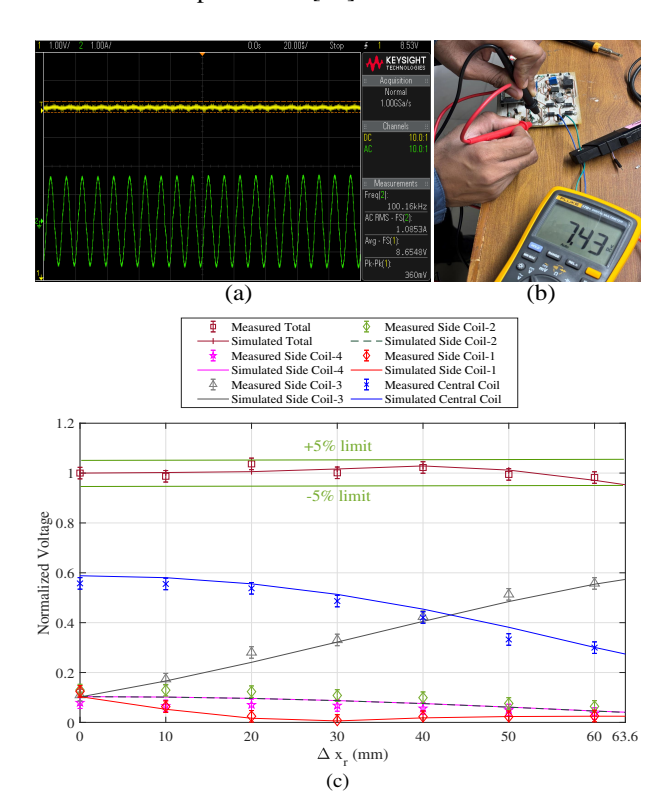
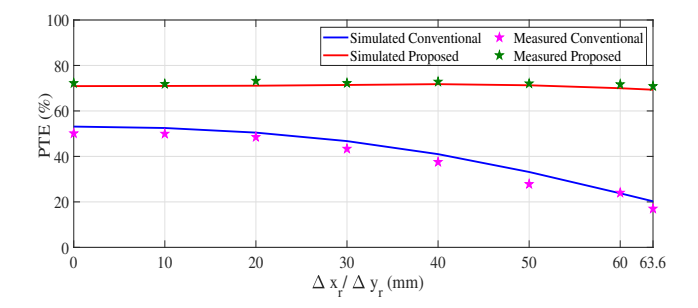


FIGURE 10. (a) Rectified voltage of RecCoil Array harvester system and Tx current waveform. (b) Voltage reading across the quadcopter battery charging point. (c) Normalized induced voltage plot in the Rx plane at 50 mm altitude due to the Tx coil of  $S_{Tx} = 127.2$  mm.

The net DC voltage of the RecCoil array harvester measured at the origin  $(V_{DC}(0,0))$  in the Keysight Digital Storage Oscilloscope (DSOX2022A) is 8.65 V for Tx coil current  $I_{TX}=1.08$  A as depicted in Fig. 10(a). The available voltage at the quadcopter battery charging point is 7.43 V, which is measured using the Fluke 17B+ Digital multimeter probe, as illustrated in Fig. 10(b). The Orange Lithium Polymer (LiPo) battery with 2200 mAh battery capacity was used for demonstrating the battery charging. The charging process

TABLE 5.	Comparison	Table for	State-of-the-Art Rx	coil designs
----------	------------	-----------	---------------------	--------------

Papers	Frequency	Rx captures	Rx coil structure	Combining Technique	Compatiblity with ICNIRP guidelines	MTA $(\Delta x_r / \Delta y_r)$	PTE (%)
[21]	28 MHz	$H_z$	Planar	No	Yes	25%	68 %
[40]	300 kHz	61.98	3-D	No	Yes	37.77%/ 11.11%	~ 80%
[24]	13.56 MHz	$H_z$	Planar	No	No	20 %	60 %
[25]	85 <i>kHz</i>	$H_x$ and $H_z$	3-D	Yes	No	22.72%	74 - 80 %
[41]	85 <i>kHz</i>	$H_x$ or $H_y$ or $H_z$	Planar	No	No	Not mentioned	77%
[42]	6.78 MHz	$H_x$ or $H_y$ or $H_z$	Planar	No	No	Not mentioned	75%
[23]	400 kHz	$H_x$ , $H_y$ , $H_z$	3-D	Yes	Yes	62 %	67.65%
[28]	1 MHz	$H_x$ , $H_y$ , $H_z$	Planar	Yes	Yes	22.86%	52.96%
Conventional Work	100 KHz	$H_z$	Planar	No	Yes	31.44 %	50.13%
Proposed Work	100 KHz	$H_x$ , $H_y$ , $H_z$	Planar	Yes	Yes	100%	72.22%



**FIGURE 11.** PTE versus misalignment along  $x_r/y_r$  axis.

took 14 minutes, during which the battery voltage increased from 2.23 V to 6.36 V. Fig. 10(c) illustrates the normalized voltage profiles with error tolerance of  $\pm 5\%$  along the  $x_r$ axis. Here, the voltages generated at each coil are normalized with respect to  $V_{DC}(0,0)$ . These profiles are symmetric about the positive and negative  $x_r/y_r$ -axes. Therefore, only the normalized profile along the positive  $x_r$ -axis is shown. The quadcopter is misaligned in steps of 10 mm up to 60 mm and at 63.6 mm from the center of the Tx coil. The voltage from the central coil decreases gradually with increasing lateral misalignment. A similar trend is seen in the voltage of side Rx coil-1 up to 30 mm, but it increases slightly thereafter. In contrast, the voltage due to Coil-3 sharply rises as it nears the Tx coil edges, capturing more of the lateral  $H_x$  field. Side coils-2 and 4 exhibit similar patterns. Notably, the total DC voltage remains nearly constant, within a  $\pm 5\%$  tolerance of lateral misalignment along  $x_r$  direction. Notably, the profiles of Coil-1 and 3 swap when misaligned towards the negative  $x_r$ -direction, with coil-2 and 4 profiles remaining nearly unaffected. Moreover, misalignment along the  $y_r$ -axis swaps the profiles of side Rx coils-1, 3, and coils-2, 4. Nonetheless, the overall rectified voltage of the RecCoil harvester system along the  $y_r$ -axis remains relatively stable, albeit with minor fluctuations due to noises present during measurement. Both measured and simulated profiles show good agreement. It is important to note that the proposed prototype is suitable for mid and large-sized quadcopters since, the load voltage is directly proportional to the Tx coil current [43].

To assess the AC to DC power transfer efficiency (PTE) of the proposed RecCoil array harvester, the output power and input power for each Rx coil are individually evaluated using their respective circuit parameters, which are then summed to compute  $P_{Lt}$  and  $P_{int}$ , correspondingly. The expression for the output power generated in each Rx coil is formulated as [44]

$$P_{L}(\Delta x_{r}, \Delta y_{r}) = \frac{(\omega_{c} M(\Delta x_{r}, \Delta y_{r}) V_{S})^{2} R_{L}}{[(R_{S} + R_{1})(R_{2} + R_{L}) + (\omega_{c} M(\Delta x_{r}, \Delta y_{r}))^{2}]^{2}}$$
(3)

In this context,  $V_S$  represents the AC source voltage applied to excite the Tx coil, while  $\omega_c$  denotes the operating frequency,  $R_1$  and  $R_2$  refer to the resistances of the Tx and Rx coils, respectively.  $M(\Delta x_r, \Delta y_r) = \frac{V_{DC}(\Delta x_r, \Delta y_r)}{\omega_c I_{Tx}}$  and  $R_L$  is taken as  $10~\Omega$  [45]. Since  $\omega_c$  and  $I_{Tx}$  are constants,  $M(\Delta x_r, \Delta y_r)$  inherently follows the same variation trend as the output voltage  $V_{DC}$ . The input power for each Rx coil is calculated using the following expression [44]

$$P_{in}(\Delta x_r, \Delta y_r) = \frac{V_S^2(R_2 + R_L)}{(R_S + R_1)(R_2 + R_L) + (\omega_c M(\Delta x_r, \Delta y_r))^2}$$
(4)

The PTE for the proposed WPT system is governed by the following expression

$$PTE = \frac{P_{Lt}}{P_{int}} \times 100\%$$
 (5)

The PTE plot versus lateral misalignment along the  $x_r/y_r$ -axis is shown in Fig. 11. It is noteworthy that the PTE at the origin increases significantly to 72.22 %, compared to a mere 50.13 % with the conventional Rx coil (i.e., only the central Rx coil capturing  $H_z$  field). This enhancement is attributed to the constructive addition of DC voltages from each Rx coil integrated with rectifier. Specifically, there is a notable 44.06 % improvement in PTE at the origin compared to the conventional Rx coil structure. Furthermore, the proposed structure shows significantly improved stability in PTE with respect to  $x_r/y_r$ -axis misalignment. The PTE for the WPT structure with the conventional Rx coil and the proposed



RecCoil array harvester under worst-case misalignment along the axis is 17.01~% and 70.91~%, respectively. This represents a dramatic improvement in PTE by 316.87~% at the Tx coil edges.

An experiment was conducted to evaluate the charging circuit's efficiency, consisting of a bridge rectifier, a DC-DC converter, and a Battery Management System (BMS). In this setup, its input port was connected to the output terminal of the inverter, with its output tested across a  $10~\Omega$  load resistor. The input AC RMS voltage of  $(V_{RMS})$  7.347 V and an RMS current  $(I_{RMS})$  of 0.3511~A were obtained at its input port. The measured DC load voltage  $(V_L)$  and current  $(I_L)$  were 4.178~V and 0.534~A, respectively. Hence, the charging circuit efficiency, accounting for the DC-DC converter and BMS, is calculated as

$$\eta_{charging} = \frac{V_L \times I_L}{V_{RMS} \times I_{RMS}} \tag{6}$$

which yields as 86.49%. For the load voltage of 7.43~V, the charging current  $(A_C)$  is obtained as 0.952~A. The duration of full charge  $(T_C)$  of battery capacity  $(C_B)$  2200~mAh LiPo battery taking into account the constant voltage charging phase is given by the following relation [46]

$$T_C = \frac{C_B}{A_C} \times 1.5 = 3.46 \, Hr$$
 (7)

In other words, it will take approximately 3 hours and 28 minutes to fully charge the Orange Lithium Polymer (LiPo) battery with a 2200 *mAh* battery capacity.

The qualitative and quantitative comparison table for stateof-the-art Rx coil structures is summarized in Table 5. [21], [24], [40] highlight Rx coils that under-utilize the available H-field generated by the Tx coil. In contrast, the approach in [25] involves a complex 3-D squirrel-cage Rx coil capturing only two H-field components. As a result, the aforementioned structures exhibit a low MTA. Furthermore, [23] employs a complex arrangement of two orthogonally tilted Rx coils that capture all three components of the H field, thus slightly improving the tolerance to misalignment. The 3-D complex structures in [23], [25], [40] suffer from poor mechanical strength, which poses challenges for integration under the quadcopter chassis. In addition, their bulky 3-D design and the adaptive LCL compensation network deployed in [41] increases the system weight, thereby reducing the drone's payload capacity. Moreover, most of the works summarized in Table 5, except [24], [25], [41], [42], comply with the ICNIRP guidelines. Although Srivastava et al. [28] proposed a planar Rx coil structure using anti-parallel coils to harvest  $H_x$  and  $H_y$ field components along with longitudinal  $H_z$  fields, the design lacks optimization for achieving decent MTA and PTE. In contrast, the proposed prototype overcomes these challenges, achieving both high PTE and 100% MTA along both axes without requiring complex phase control of Tx coil currents as performed in [42]. Moreover, the proposed RecCoil array harvester structure weighs merely 270 g, which is less than the prescribed weight of 290 g for the Rx coil to be placed under drone chassis [9], [47].

### **V. CONCLUSION**

This manuscript proposes an innovative on-body RecCoil array harvester system for wireless quadcopter charging applications. The design features a central Rx coil placed beneath the quadcopter's central body to capture longitudinal fields and a planar four-side Rx coils containing two oppositely winded circular coils mounted at the quadcopter's landing gear to capture lateral fields. These coils are integrated with a full-bridge rectifier to produce a DC output voltage for wirelessly charging the quadcopter's battery. Through systematic optimization of the Tx, central, and side Rx coils, a uniform load voltage and a nearly constant Power Transfer Efficiency (PTE) across the horizontal and vertical Rx plane dimensions (X and Y axes) are achieved, thereby fulfilling misalignmentoblivious wireless quadcopter charging, an accomplishment not attained in the state-of-the-art literary works. This result is verified experimentally by prototyping the proposed structure with Litz wire. The experimental measurements were limited to static tests, during which the quadcopter was held stationary with the proposed Rx coils mounted underneath to measure rectified voltage and calculate power transfer efficiency at distinct points along X and Y axes. Notably, the proposed RecCoil array harvester structure significantly improved the measured PTE to 72.22 % under aligned conditions and 70.91 % under worst-case misalignment along the axis, compared to just 50.13% and 17.01%, respectively, for conventional Rx coils. The rectified DC voltage of the Rec-Coil Array harvester is then integrated with the PCB-based charging circuitry to demonstrate successful charging of the quadcopter battery. Furthermore, the realized planar structure using Litz wire is also lightweight, minimally affecting the quadcopter payload capacity and demonstrating the considerable potential for efficient wireless quadcopter charging over extended regions. Compared to 3-D designs in [23], [25] and [40] in Table 5, which report PTE of 67.65%, 80% with MTAs of only 62 %, 22.72% and 37.77% respectively, the proposed work achieves comparable efficiency while offering significantly higher misalignment tolerance. Similarly, planar coils in [24] and [28] provide lower efficiencies of 60% and 52.96\% with poor MTA. These results exemplify that the proposed structure uniquely combines high efficiency and planar simplicity. Furthermore, it achieves complete misalignment tolerance along the axes, making it a robust and practical solution for drone charging applications. The proposed structure is scalable to charge higher-voltage batteries for larger UAVs and can be adapted for diverse aerial applications. Future work will focus on optimizing the charging circuitry involving ESP32-based control circuit and relay system to improve the overall system efficiency by reducing losses in the DC-DC converter and battery management system, performing actual drone landing tests to validate the proposed Rx coil structure for real charging applications and assessing the durability of Litz wires and rectifier diodes under variable temperature and mechanical loading conditions.

S. Jain et al.: An On-body RecCoil Array Harvester System for Extended Wireless Charging of Misaligned Quadcopters

## **REFERENCES**

- C. J. Li and H. Ling, "An Investigation on the Radar Signatures of Small Consumer Drones," *IEEE Antennas and Wireless Propagation Letters*, vol. 16, pp. 649–652, 2017.
- [2] Z. Akhter, R. M. Bilal, and A. Shamim, "A Dual Mode, Thin and Wideband MIMO Antenna System for Seamless Integration on UAV," *IEEE Open Journal of Antennas and Propagation*, vol. 2, pp. 991–1000, 2021.
- [3] M. Y. Arafat and S. Moh, "JRCS: Joint Routing and Charging Strategy for Logistics Drones," *IEEE Internet of Things Journal*, pp. 1–1, 2022.
- [4] J. Liang, B. I. Ahmad, M. Jahangir, and S. Godsill, "Detection of Malicious Intent in Non-cooperative Drone Surveillance," in 2021 Sensor Signal Processing for Defence Conference (SSPD), 2021, pp. 1–5.
- [5] P. K. Chittoor, B. Chokkalingam, and L. Mihet-Popa, "A Review on UAV Wireless Charging: Fundamentals, Applications, Charging Techniques and Standards," *IEEE Access*, vol. 9, pp. 69 235–69 266, 2021.
- [6] A. Eid, N. Rich, A. Hattori, I.-T. Chen, J. Hester, and M. M. Tentzeris, "Deployable Origami Coils for Wireless UAV in-Flight Powering," in 2023 IEEE Wireless Power Technology Conference and Expo (WPTCE). IEEE, 2023, pp. 1–4.
- [7] Y. Shao, N. Kang, H. Zhang, R. Ma, M. Liu, and C. Ma, "A Lightweight and Robust Drone MHz WPT System via Novel Coil Design and Impedance Matching," *IEEE Transactions on Industry Applications*, 2023.
- [8] Y. Li, W. Sun, J. Liu, Y. Liu, X. Yang, Y. Li, J. Hu, and Z. He, "A new magnetic coupler with high rotational misalignment tolerance for unmanned aerial vehicles wireless charging," *IEEE Transactions on Power Electronics*, vol. 37, no. 11, pp. 12986–12991, 2022.
- [9] A. M. Jawad, H. M. Jawad, R. Nordin, S. K. Gharghan, N. F. Abdullah, and M. J. Abu-Alshaeer, "Wireless Power Transfer With Magnetic Resonator Coupling and Sleep/Active Strategy for a Drone Charging Station in Smart Agriculture," *IEEE Access*, vol. 7, pp. 139 839–139 851, 2019.
- [10] P. K. Chittoor and C. Bharatiraja, "Wireless-Sensor Communication Based Wireless-Charging Coil Positioning System for UAVs With Maximum Power Point Tracking," *IEEE Sensors Journal*, vol. 22, no. 8, pp. 8175– 8182, 2022.
- [11] B. M. Mosammam and M. Mirsalim, "New integrated tripolar pad using double-sided lcc compensation for wireless power transfer," *IEEE Trans*actions on Vehicular Technology, vol. 69, no. 12, pp. 15 633–15 643, 2020.
- [12] Y. Gu, J. Wang, Z. Liang, and Z. Zhang, "Mutual-Inductance-Dynamic-Predicted Constant Current Control of LCC-P Compensation Network for Drone Wireless In-Flight Charging," *IEEE Transactions on Industrial Electronics*, vol. 69, no. 12, pp. 12710–12719, 2022.
- [13] F. Xu, S. Wei, J. Li, D. Yuan, and K. Chen, "Investigation on Compensation Topology and Its Parameter Matching Method for Dynamic Wireless Power Transfer System," *IEEE Transactions on Industry Applications*, vol. 60, no. 4, pp. 5692–5701, 2024.
- [14] Al Mahmud, Shamsul Arefeen and Panhwar, Ishtiaque and Jayathurathnage, Prasad, "Large-Area Free-Positioning Wireless Power Transfer to Movable Receivers," *IEEE Transactions on Industrial Electronics*, vol. 69, no. 12, pp. 12807–12816, 2022.
- [15] P. Yadav and M. Veerachary, "Modified Coupler with Reduced Misalignment Issues for Wireless Power Transfer System," *IEEE Transactions on Industry Applications*, pp. 1–15, 2024.
- [16] A. Bharadwaj, A. Sharma, and C. C. Reddy, "A Multi-turn Coil Antenna with Non-uniform Clustered Turns Optimized using Q-assisted MMSE Procedure to Enhance Misalignment Tolerance in WPT Systems," *IEEE Transactions on Antennas and Propagation*, pp. 1–1, 2022.
- [17] Y. Shao, N. Kang, H. Zhang, R. Ma, M. Liu, and C. Ma, "A Lightweight and Robust Drone MHz WPT System via Novel Coil Design and Impedance Matching," *IEEE Transactions on Industry Applications*, vol. 59, no. 3, pp. 3851–3864, 2023.
- [18] W. Han, K. T. Chau, C. Jiang, W. Liu, and W. H. Lam, "Design and Analysis of Quasi-Omnidirectional Dynamic Wireless Power Transfer for Fly-and-Charge," *IEEE Transactions on Magnetics*, vol. 55, no. 7, pp. 1–9, 2019.
- [19] A. Bharadwaj, V. K. Srivastava, A. Sharma, and C. C. Reddy, "A Switchable Multicoil Antenna With Booster Coil to Improve Coverage in WPT Systems," *IEEE Transactions on Antennas and Propagation*, vol. 70, no. 4, pp. 2490–2498, 2022.
- [20] A. Bharadwaj, A. Sharma, and C. R. Chandupatla, "A Switched Modular Multi-Coil Array Transmitter Pad With Coil Rectenna Sensors to Improve Lateral Misalignment Tolerance in Wireless Power Charging of Drone Systems," *IEEE Transactions on Intelligent Transportation Systems*, vol. 24, no. 2, pp. 2010–2023, 2023.

- [21] A. Eid, N. Rich, A. Hattori, I.-T. Chen, J. Hester, and M. M. Tentzeris, "Deployable Origami Coils for Wireless UAV in-Flight Powering," in 2023 IEEE Wireless Power Technology Conference and Expo (WPTCE), 2023, pp. 1–4.
- [22] C. Rong, X. He, Y. Wu, Y. Qi, R. Wang, Y. Sun, and M. Liu, "Optimization Design of Resonance Coils With High Misalignment Tolerance for Drone Wireless Charging Based on Genetic Algorithm," *IEEE Transactions on Industry Applications*, vol. 58, no. 1, pp. 1242–1253, 2022.
- [23] A. Bharadwaj, V. K. Srivastava, A. Sharma, and C. C. Reddy, "A Tilted-Orthogonal Receiver Coil Antenna to Improve Misalignment Tolerance in WPT Systems," *IEEE Transactions on Antennas and Propagation*, vol. 70, no. 12, pp. 11434–11441, 2022.
- [24] J. M. Arteaga, S. Aldhaher, G. Kkelis, C. Kwan, D. C. Yates, and P. D. Mitcheson, "Dynamic Capabilities of Multi-MHz Inductive Power Transfer Systems Demonstrated With Batteryless Drones," *IEEE Transactions on Power Electronics*, vol. 34, no. 6, pp. 5093–5104, 2019.
- [25] P. Cao, Y. Lu, H. Zhang, J. Li, W. Chai, C. Cai, and S. Wu, "Embedded Lightweight Squirrel-Cage Receiver Coil for Drone Misalignment-Tolerant Wireless Charging," *IEEE Transactions on Power Electronics*, vol. 38, no. 3, pp. 2884–2888, 2023.
- [26] T. Campi, S. Cruciani, F. Maradei, and M. Feliziani, "Efficient Wireless Drone Charging Pad for Any Landing Position and Orientation," *Energies*, vol. 14, no. 23, p. 8188, 2021.
- [27] S. Jain, A. Bharadwaj, and A. Sharma, "A Mortarboard-Shaped Receiver Antenna for Drone Wireless Charging to Achieve an Outspread Misalignment Tolerance Towards Imperfect Landing," *IEEE Transactions on Vehicular Technology*, vol. 74, no. 1, pp. 61–73, 2025.
- [28] V. K. Srivastava, A. Bharadwaj, and A. Sharma, "A Planar Distributed Receiver Coil Antenna Array to Encapsulate Vertical and Lateral H-Fields for Drone Wireless Charging," in 2023 17th European Conference on Antennas and Propagation (EuCAP), 2023, pp. 1–5.
- [29] W.-S. Lee, H.-S. Jang, K.-S. Oh, and J.-W. Yu, "Close Proximity Effects of Metallic Environments on the Antiparallel Resonant Coil for Near-Field Powering," *IEEE Transactions on Antennas and Propagation*, vol. 61, no. 6, pp. 3400–3403, 2013.
- [30] W.-S. Lee, W.-I. Son, K.-S. Oh, and J.-W. Yu, "Contactless Energy Transfer Systems Using Antiparallel Resonant Loops," *IEEE Transactions on Industrial Electronics*, vol. 60, no. 1, pp. 350–359, 2013.
- [31] V. K. Srivastava, A. Sharma, and A. Bharadwaj, "A Planar Distributed Multicoil Antenna to Generate 3-D Ellipsoidally Polarized H-Field for Angular Misalignment Tolerant WPT System," *IEEE Transactions on Antennas and Propagation*, vol. 70, no. 4, pp. 2969–2978, 2022.
- [32] C. A. Balanis, Antenna Theory: Analysis and Design. John wiley & sons, 2016.
- [33] A. S. AlShahri, M. T. Nguyet Dinh, and N. K. C. Nair, "Induced voltage on pipeline located close to high voltage lines due to electromagnetic induction," in 2014 Australasian Universities Power Engineering Conference (AUPEC), 2014, pp. 1–5.
- [34] A. M. Jawad, R. Nordin, S. K. Gharghan, H. M. Jawad, and M. Ismail, "Opportunities and Challenges for Near-Field Wireless Power Transfer: A Review," *Energies*, vol. 10, no. 7, 2017. [Online]. Available: https://www.mdpi.com/1996-1073/10/7/1022
- [35] A. Bharadwaj, V. K. Srivastava, C. C. Reddy, and A. Sharma, "Design Methodology of Near-Field Transmitter Coil Antenna for Maximizing Efficiency of the WPT System," in 2023 17th European Conference on Antennas and Propagation (EuCAP), 2023, pp. 1–5.
- [36] U. Gordhan and S. Jayalath, "Wireless Power Transfer System for an Unmanned Aerial Vehicle," in 2021 12th Power Electronics, Drive Systems, and Technologies Conference (PEDSTC), 2021, pp. 1–5.
- [37] Product Catalogue: Litz Wire, Parashar Vidyut Udyog, Noida, India, 2025.
- [38] C. Rong, X. Duan, M. Chen, Q. Wang, L. Yan, H. Wang, C. Xia, X. He, Y. Zeng, and Z. Liao, "Critical Review of Recent Development of Wireless Power Transfer Technology for Unmanned Aerial Vehicles," *IEEE Access*, vol. 11, pp. 132 982–133 003, 2023.
- [39] S. Jiao, G. Zhang, M. Zhou, and G. Li, "A Comprehensive Review of Research Hotspots on Battery Management Systems for UAVs," *IEEE Access*, vol. 11, pp. 84636–84650, 2023.
- [40] T. Campi, S. Cruciani, F. Maradei, and M. Feliziani, "Innovative Design of Drone Landing Gear Used as a Receiving Coil in Wireless Charging Application," *Energies*, vol. 12, no. 18, 2019. [Online]. Available: https://www.mdpi.com/1996-1073/12/18/3483
- [41] Y. Yao, Y. Wang, X. Liu, Y. Pei, D. Xu, and X. Liu, "Particle Swarm Optimization-Based Parameter Design Method for S/CLC-Compensated IPT Systems Featuring High Tolerance to Misalignment and Load Varia-



- tion," *IEEE Transactions on Power Electronics*, vol. 34, no. 6, pp. 5268–5282, 2019.
- [42] N. Kang, H. Qin, R. Ma, C. H. T. Lee, M. Liu, and C. Ma, "Magnetic Field Projection and Current Phase Control in a 2-D Planar Transmitting Coil Array," *IEEE Transactions on Power Electronics*, vol. 39, no. 9, pp. 10623–10637, 2024.
- [43] S. Huh and D. Ahn, "Two-Transmitter Wireless Power Transfer with Optimal Activation and Current Selection of Transmitters," *IEEE Transactions on Power Electronics*, vol. 33, no. 6, pp. 4957–4967, 2018.
- [44] S. Wang, Z. Hu, C. Rong, C. Lu, J. Chen, and M. Liu, "Planar Multiple-Antiparallel Square Transmitter for Position-Insensitive Wireless Power Transfer," *IEEE Antennas and Wireless Propagation Letters*, vol. 17, no. 2, pp. 188–192, 2018.
- [45] J. Zhou, B. Zhang, W. Xiao, D. Qiu, and Y. Chen, "Nonlinear Parity-Time-Symmetric Model for Constant Efficiency Wireless Power Transfer: Application to a Drone-in-Flight Wireless Charging Platform," *IEEE Transactions on Industrial Electronics*, vol. 66, no. 5, pp. 4097–4107, 2019.
- [46] Ufine Battery, "Lipo battery charge rate calculator," https://www.ufinebattery.com/blog/lipo-battery-charge-rate-calculator/, Aug. 2025.
- [47] L. Yu, L. Wu, Y. Zhu, X. Cao, G. Zhang, and S. Xiang, "Wireless charging concave coil design for UAVs," *Electronics*, vol. 11, no. 13, p. 1962, 2022.



**SAGAR JAIN** (Graduate Student Member, IEEE) received the B.Tech. degree in Electronics and Communication Engineering with minor in mathematics from Shiv Nadar Institution of Eminence, Greater Noida, Uttar Pradesh, India, in 2016, and the M.Tech. degree in electronics and communication engineering from the Indraprastha Institute of Information Technology, New Delhi, Delhi, India, in 2019. He is currently pursuing the Ph.D. degree with the Electrical Engineering Department,

Indian Institute of Technology Ropar, Rupnagar, Punjab, India. His current research interest include near-field wireless power transfer.



## $\textbf{IGNACIO JULIO GARCIA ZUAZOLA} \ (M'11-SM'15)$

completed a PhD in Electronics (Antennas) parttime program in 2008; viva in 2010, University of Kent, Canterbury, UK, an eMBA in Business (part-time program) in 2016, Cardiff Metropolitan University, UK, a BENG in Telecommunications Engineering in 2003, Queen Mary - University of London, a HND in Telecommunications Engineering in 2000, North West London - University of Middlesex and a FPII in Industrial Electronics in

1995, School of Chemistry Electronics of Indautxu, Spain. Has academic experience and been employed as Research Associate (2004) University of Kent, Research Engineer, Grade 9/9 (2006) University of Wales, Swansea, UK, Research Associate (2008) University of Kent, Senior Research Fellow (2011) University of Deusto, Bilbao, Spain, Visiting Senior Research Fellow (2011) University of Leeds, UK, Research Associate (2014) Loughborough University, UK, Representative of Spain (2015) London School of Commerce, UK, Lecturer in Electronic Engineering (2018) University of Portsmouth, UK. Holds educational awards in Electricity, Pneumatic Hydraulics and Robotics and possesses relevant industrial experience, been hired for Babcok Wilcox (1993), Iberdrola (1995), Telefonica (1997), Thyssen Elevators (1998), Cell Communications (2000), Nokia Bell Labs (2020) and Bilbao Ekintza - Bilbao City Council (2021) and engaged in a SME in electrical wiring (1996). He was a Senior Lecturer (2022) and currently a Reader in Electronic Engineering (2024) London Metropolitan University (London Met), UK. Included in Marquis Who's Who in the World 2010 edition, has published in international journals: IEEE Transactions, IET Proceedings and Electronics Letters. Current research interests include business development on one hand and single-band and multiband miniature antennas, and the use of Electromagnetic-Band Gap (EBG) structures and Frequency-Selective Surfaces (FSS). He led the antennas research line and supervised and mentored graduate and postgraduate students and currently bids for grants and contributes to the teaching, scientific, technological and business development of London Met by promoting and increasing branding, research and innovation. He is a MIET, a SMIEEE and a SFHEA.



**ASHWANI SHARMA** (Senior Member, IEEE) received the B.Tech. degree from The LNM Institute of Information Technology, Jaipur, India, in 2010, the master's degree in technology and communication systems from the Escuela Tecnica Superior de Ingenieros de Telecomunicacion (ETSIT), Technical University of Madrid (UPM), Madrid, Spain, in 2013, and the Ph.D. degree from the University of Deusto, Bilbao, Spain, in 2015. He was a Junior Research Fellow with IIT Delhi, New Delhi, India,

from 2010 to 2011, and a Visiting Training Fellow with the University of Kent, Canterbury, U.K., from May 2014 to August 2014. He has been working as an Assistant Professor with IIT Ropar, Rupnagar, India, since July 2018. His research works have been published in various international journals and conferences, such as IEEE Transactions and Letters, IET journals, and Wiley letters. His current research interests include exploiting field-forming techniques in antenna design for wireless power transmission, the IoT, and 5G.

. . .